

Helium-like triplet density diagnostics

Applications to CHANDRA–LETGS X-ray observations of Capella and Procyon

J.-U. Ness¹, R. Mewe², J. H. M. M. Schmitt¹, A. J. J. Raassen^{2,3}, D. Porquet⁴,
J. S. Kaastra², R. L. J. van der Meer², V. Burwitz⁵, and P. Predehl⁵

¹ Universität Hamburg, Gojenbergsweg 112, 21029 Hamburg, Germany

² Space Research Organization Netherlands (SRON), Sorbonnelaan 2, 3584 CA Utrecht, The Netherlands

³ Astronomical Institute “Anton Pannekoek”, Kruislaan 403, 1098 SJ Amsterdam, The Netherlands

⁴ CEA/DSM/DAPNIA, Service d’Astrophysique, CEA Saclay, 91191 Gif-sur-Yvette Cedex, France

⁵ Max-Planck-Institut für Extraterrestrische Physik (MPE), Postfach 1603, 85740 Garching, Germany

Received 18 September 2000 / Accepted 1 December 2000

Abstract. Electron density diagnostics based on the triplets of helium-like C V, N VI, and O VII are applied to the X-ray spectra of Capella and Procyon measured with the Low Energy Transmission Grating Spectrometer (LETGS) on board the Chandra X-ray Observatory. New theoretical models for the calculation of the line ratios between the forbidden (f), intercombination (i), and the resonance (r) lines of the helium-like triplets are used. The (logarithmic) electron densities (in cgs units) derived from the f/i ratios for Capella are $< 9.38 \text{ cm}^{-3}$ for O VII (2σ upper limit) ($f/i = 4.0 \pm 0.25$), $9.86 \pm 0.12 \text{ cm}^{-3}$ for N VI ($f/i = 1.78 \pm 0.25$), and $9.42 \pm 0.21 \text{ cm}^{-3}$ for C V ($f/i = 1.48 \pm 0.34$), while for Procyon we obtain $9.28_{-9.28}^{+0.4} \text{ cm}^{-3}$ for O VII ($f/i = 3.28 \pm 0.3$), $9.96 \pm 0.23 \text{ cm}^{-3}$ for N VI ($f/i = 1.33 \pm 0.28$), and $< 8.92 \text{ cm}^{-3}$ for C V ($f/i = 0.48 \pm 0.12$). These densities are quite typical of densities found in the solar active regions, and also pressures and temperatures in Procyon’s and Capella’s corona at a level of $T \sim 10^6 \text{ K}$ are quite similar. We find no evidence for densities as high as measured in solar flares. Comparison of our Capella and Procyon measurements with the Sun shows little difference in the physical properties of the layers producing the C V, N VI, and O VII emission. Assuming the X-ray emitting plasma to be confined in magnetic loops, we obtain typical loop length scales of $L_{\text{Capella}} \geq 8 L_{\text{Procyon}}$ from the loop scaling laws, implying that the magnetic structures in Procyon and Capella are quite different. The total mean surface fluxes emitted in the helium- and hydrogen-like ions are quite similar for Capella and Procyon, but exceed typical solar values by one order of magnitude. We thus conclude that Procyon’s and Capella’s coronal filling factors are larger than corresponding solar values.

Key words. atomic data – atomic processes – techniques: spectroscopic – stars: individual: Capella & Procyon – stars: coronae – stars: late-type – stars: activity – X-rays: stars

1. Introduction

The hot plasma in the corona of the Sun and of other stars is thought to be in “coronal equilibrium”. Atomic excitations occur through collisions with electrons. The excited atoms decay radiatively and the emitted radiation escapes without any further interaction with the emitting plasma. As a consequence, the emission is optically thin, and the total flux emitted in some spectral band or in a given emission line is proportional to the emission measure EM , defined as the integral of the square of the plasma density n over the emitting volume elements dV through

$EM = \int n^2 dV$. Thus, observationally, the contributions of density and volume to a given observed value of EM cannot be disentangled.

Stellar X-ray surveys carried out with the *Einstein* and ROSAT satellites have shown an enormous range of X-ray luminosity (L_X) for stars of given spectral type (cf., Vaiana et al. 1981; Schmitt 1997). Typically, one observes star to star variations in L_X of up to four orders of magnitude, with the largest X-ray luminosities found among the stars with the largest rotation rates. While one definitely finds a correlation between mean coronal temperature and X-ray luminosity (Schmitt et al. 1985; Schmitt 1997), it is also clear that the single-most important factor contributing to the large variations in L_X is the variation in

Send offprint requests to: J.-U. Ness,
e-mail: jness@hs.uni-hamburg.de

emission measure. The conclusion therefore is that active stars (can) have a couple of orders of magnitude higher coronal emission measure, while maintaining the same optical output as low-activity stars like our Sun.

The emission measure is directly linked to the structure of stellar coronae, if we assume, going along with the solar analogy, that the X-ray emitting plasma of a stellar corona is confined in magnetic loops. The observed values of EM and L_X for a given star could be accounted for either by the existence of more loops than typically visible on the solar surface, by higher density loops or by longer, more voluminous loops. Thus the question is reduced to the following: if $EM_\star \gg EM_\odot$ for an active star, one wants to know whether this is due to $n_\star > n_\odot$ or $V_\star > V_\odot$ or both.

Spatially resolved solar observations allow to disentangle density and volume contributions to the overall emission measure. One finds the total X-ray output of the Sun dominated – at least under maximum conditions – by the emission from rather small, dense loops. Stellar coronae always appear as point sources. The only way to infer structural information in these unresolved point sources has been via eclipse studies in suitably chosen systems where one tries to constrain the emitting plasma volume from the observed light curve. Another method to infer structure in spatially unresolved data are spectroscopic measurements of density. The emissivity of plasma in coronal equilibrium in carefully selected lines does depend on density. Some lines may be present in low-density plasmas and disappear in high-density plasmas such as the forbidden lines in He-like triplets, while other lines may appear in high-density plasmas and be absent in low-density plasmas (such as lines formed following excitations from excited levels). With the high-resolution spectroscopic facilities onboard *Chandra* it is possible to carry out such studies for a wide range of X-ray sources. The purpose of this paper is to present and discuss some key density diagnostics available in the high-resolution grating spectra obtained with *Chandra*. We will specifically discuss the spectra obtained with the Low Energy Transmission Grating Spectrometer (LETGS) for the stars Capella and Procyon.

Both Capella and Procyon are known to be relative steady and strong X-ray sources; no signatures of flares from these stars have ever been reported in the literature. Both Capella and Procyon are rather close to the Sun at distances of 13 pc and 3.5 pc (Table 1), so that effects of interstellar absorption are very small. Both of them have been observed with virtually all X-ray satellites flown so far. Capella was first detected as an X-ray source by Catura et al. (1975), and confirmed by Mewe et al. (1975), Procyon by Schmitt et al. (1985). The best coronal spectra of Capella were obtained with the *Einstein* Observatory FPCS and OGS (Vedder et al. 1983; Mewe et al. 1982), the EXOSAT transmission grating (Mewe et al. 1986; Lemen et al. 1989) and EUVE (Dupree et al. 1993; Schrijver et al. 1995), while high-spectral resolution spectral data for Procyon have been presented by Mewe et al. (1986) and

Table 1. Properties of Procyon and Capella: mass M , radius R , effective temperature T_{eff} , $\log g$ and the limb darkening coefficient ϵ

	Procyon	Capella
d/pc	3.5	13
M/M_\odot	1.7 ± 0.1^4	2.56 ± 0.04^3
R/R_\odot	2.06 ± 0.03^4	9.2 ± 0.4^3
T_{eff}/K	6530 ± 90^2	5700 ± 100^3
$\log g$	4.05 ± 0.04^2	2.6 ± 0.2^5
Spectr. type	F5 IV–V	Ab: G1 III (Aa: G8/K0 III)
ϵ	0.724^1	0.83^1

References:

¹Díaz-Cordovés et al. (1995).

²Fughrman et al. (1997).

³Hummel et al. (1994).

⁴Irwin et al. (1992).

⁵Kelch et al. (1978).

Lemen et al. (1989) using EXOSAT transmission grating data and Drake et al. (1995) and Schrijver et al. (1995) using EUVE data. Note that Schmitt et al. (1996b) and Schrijver et al. (1995) investigated the coronal density of Procyon using a variety of density sensitive lines from Fe X to Fe XIV in the EUV range and found Procyon’s coronal density consistent with that of solar active region densities.

The plan of our paper is as follows: We first briefly review the atomic physics of He-like ions as applicable to solar (and our stellar) X-ray spectra. We briefly describe the spectrometer used to obtain our data, and discuss in quite some detail the specific procedures used in the data analysis, since we plan to use these methods in all our subsequent work on *Chandra* and XMM-Newton spectra. We then proceed to analyze the extracted spectra and describe in detail how we dealt with the special problem of line blending with higher dispersion orders. Before presenting our results we estimate the formation temperatures of the lines, the influence of the stellar radiation field and the influence of optical depth effects followed by detailed interpretation. The results will then be compared to measurements of the Sun and we close with our conclusions.

2. Atomic physics of He-like ions

The theory of the atomic physics of helium-like triplets has been extensively described in the literature (Gabriel & Jordan 1969; Blumenthal et al. 1972; Mewe & Schrijver 1978; Pradhan et al. 1981; Pradhan & Shull 1981; Pradhan 1982; Pradhan 1985, and recently Porquet & Dubau 2000; Mewe et al. 2000a). Basically, the excited states ($1s2l$) split up into the terms 2^1P , 2^3P , 2^1S , and 2^3S , out of which the levels with $J \neq 0$ decay to the ground state 1^1S through the resonance line (abbreviated

by r), the intercombination line (i) and the forbidden line (f), respectively; the latter two lines involve spin changes and therefore violate the selection rules for electric dipole radiation. Although the radiative transition rate for the forbidden line is quite small, in a low-density plasma collisional depopulation processes are so rare, that the excited 2^3S state does decay radiatively. In a high-density plasma collisional deexcitations dominate and hence the forbidden line disappears. Complications arise from other competing processes populating and depopulating the $3P$ and $3S$ levels. These are in particular radiative transitions induced by the underlying photospheric stellar radiation field (discussed in Sect. 5.2) as well as ionization and recombination processes from the Li-like and H-like ions.

It is customary to describe the measured line intensities r , i and f in terms of the ratios

$$R_{\text{obs}} = \frac{f}{i} \quad \text{and} \quad G_{\text{obs}} = \frac{i+f}{r}. \quad (1)$$

In this paper we use the notation used in e.g. Pradhan & Shull (1981). In other contexts (e.g. calculating ions of higher ionization stages) another notation labeling r as w , f as z and i as $x+y$ is often used pointing out that the intercombination line separates via M2 and E1 transitions into two components. Theory describes the density sensitivity of the R ratio by the functional dependence

$$R(N_e) = R_0 \frac{1}{1 + \phi/\phi_c + N_e/N_c}. \quad (2)$$

Densities are inferred from equating $R(N_e)$ with R_{obs} . For convenience, we follow here the expressions as given by (1972). The low-density limit R_0 , which applies for $N_e = 0$ and $\phi = 0$, is given by

$$R_0 = \frac{1+F}{B} - 1, \quad (3)$$

with the radiative branching parameter B averaged over the two components of the intercombination line. The parameter N_c , the so-called critical density (cf., Table 2), above which the observed line ratio is density-sensitive, is given by

$$N_c = \frac{A(2^3S_1 \rightarrow 1^1S_0)}{(1+F)C(2^3S_1 \rightarrow 2^3P)}, \quad (4)$$

where $A(2^3S_1 \rightarrow 1^1S_0)$ is the radiative transition probability of the forbidden line, $C(2^3S_1 \rightarrow 2^3P)$ is the electron collisional rate coefficient for the transition from 2^3S to 2^3P , and F is the ratio of the collision rates from the ground to the levels 2^3S and 2^3P , respectively (including cascade effects from upper levels through radiative transitions after excitation or recombination). Finally, the parameters ϕ (the radiative absorption rate from 2^3S to 2^3P induced by an external radiation field) and ϕ_c describe the additional possible influence of the stellar radiation field on the depopulation of the $3S$ state (cf., Sect. 5.2). The latter is insignificant especially for the He-like triplets of higher ionization stages than C v. Values for R_0 and N_c used in this paper are listed in Table 2. Obviously, for very

Table 2. Atomic parameters for He-like triplets. T_m is the peak line formation temperature (MEKAL), R_0 is the low-density limit and N_c the density where R falls to half its low-density value

ion	T_m/MK	R_0	$N_c/(10^{10} \text{ cm}^{-3})$
C v	1	10.6	0.051
N vi	1.4	4.9	0.45
O vii	2.0	3.495	3.00

large densities or large radiation fields the forbidden line and hence R disappears. The ratio

$$G = (i+f)/r, \quad (5)$$

a measure of the relative strength of the resonance line, depends on the electron temperature, T_e (e.g., Mewe et al. 2000a). G can be used to derive temperatures for the lines used for density diagnostics that can be compared to the maximum formation temperature T_m .

3. Instrument description

The Low Energy Transmission Grating Spectrometer (LETGS) on board the Chandra Observatory is a diffraction grating spectrometer covering the wavelength range between 2–175 Å (0.07–6 keV). 540 individual grating elements are mounted onto a toroidal ring structure. Each of the elements consists of a freestanding gold grating with 1 μm grating period. The fine gold wires are held by two different support structures, a linear grid with 25.4 μm and a coarse triangular mesh with 2 mm spacing. The whole grating can be inserted into the convergent beam just behind the High Resolution Mirror Assembly (HRMA) thereby dispersing the light of any X-ray source in the field of view into its spectrum. The efficiency of the grating spectrometer is of the order of 10% on average but is enhanced by a factor of two around 2 keV due to partial transparency effects; a more detailed description of the instrument is presented by Predehl et al. (1997). Both sides of the spectrum are recorded with a microchannel plate detector (HRCS), placed behind the transmission grating. In contrast to CCD based detectors, the HRCS detector provides essentially no intrinsic energy resolution, the energy information for individually recorded events is solely contained in the events' spatial location.

4. Observations and data analysis

4.1. Observations

The data described and analyzed in this paper were gathered during the calibration phase of the *Chandra* LETGS. Part of the data has already been presented by Brinkman et al. (2000). The individual observation intervals used in our analysis are listed in Table 3. As is clear from Table 3, the observations extend over two days for Procyon and over two months for Capella. Our analysis refers to

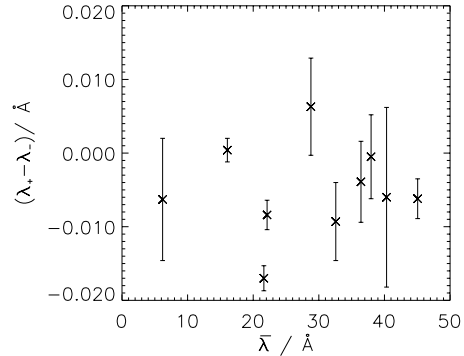
Table 3. List of the data sets with start and stop times and durations used in this paper

Obs. ID.	time [ksec]	Observation date [UT]	
		start	end
Capella			
62435	22.34	09-06-1999 00:35:40	09-06-1999 06:48:01
01167	15.36	09-09-1999 13:10:06	09-09-1999 17:26:08
01244	12.37	09-09-1999 17:42:27	09-09-1999 21:08:36
62410	11.33	09-09-1999 23:43:57	09-10-1999 02:52:48
01246	15.00	09-10-1999 03:06:06	09-10-1999 07:16:08
62422	11.68	09-12-1999 18:26:42	09-12-1999 21:41:20
62423	14.80	09-12-1999 23:37:44	09-13-1999 03:44:28
01420	30.30	10-29-1999 22:49:29	10-30-1999 07:14:27
01248	85.36	11-09-1999 13:42:24	11-10-1999 13:25:05
total:	218.54		
Procyon			
00063	70.39	11-06-1999 21:24:31	11-07-1999 16:57:38
01461	70.36	11-07-1999 17:04:55	11-08-1999 12:37:39
total:	140.75		

the mean properties of Procyon and Capella; the subject of possible time variations is not subject of this paper. The total on source integration times are 218.54 ksec for Capella and 140.75 ksec for Procyon. Since the sources are among the strongest coronal X-ray sources (cf., Hünsch et al. 1998a,b), it is also evident that these spectra belong to the highest quality coronal X-ray spectra reasonably obtainable with the *Chandra* LETGS.

4.2. Data extraction

All the HRCS datasets analyzed in this paper (see Table 3) were processed using the standard pipeline processing. The incoming X-rays are diffracted by the grating, dispersing the different energy photons to different detector positions along the dispersion direction. Therefore the spectral information obtained with the LETGS has to be extracted spatially. The pulse heights with which the HRC detector records registered events contains some very modest energy information, which was, however, not used. At each wavelength, the photons have to be integrated in cross-dispersion direction. Because of the spectrograph's astigmatism, the width of the spectral trace in cross-dispersion direction is wavelength dependent. For wavelengths below 75 Å we choose a 3.6'' wide extraction box around the spectral trace which includes almost all of the source signal while keeping the background level low. For wavelengths greater than 75 Å the extraction box widens in cross dispersion direction to 8.4'' at 175 Å. In addition the photons in four background regions of identical shape to that of the object extraction region where selected. These regions are displaced 12'' and 24'' above and below the source

**Fig. 1.** Comparison of fit results from left side (λ_-) and right side (λ_+) of the spectrum

extraction box in order to check for any spatial variation of the background in cross-dispersion direction.

4.3. Symmetry of the grating spectrum

For the purpose of verifying the symmetry of the dispersed spectra, we determined empirical wavelengths of ten strong emission lines recorded on both sides of the middle detector plate (i.e. $\lambda < 50$ Å). For the example of Capella we plot the wavelength difference ($\lambda_+ - \lambda_-$) against the mean wavelength $\frac{1}{2}(\lambda_+ + \lambda_-)$ in Fig. 1. As can be seen from Fig. 1, the wavelength values obtained from the right and left side agree to within less than the instrumental resolution of ~ 0.06 Å (cf. σ -values in Table 4). Both spectra can thus be added for the analysis in order to increase the SNR of the data. In the following we will always consider co-added spectra.

4.4. Method of analysis

4.4.1. Treatment of background

Before determining the flux of any emission line, the spectral background must be modeled. This background consists of essentially two components: instrumental background and source background, which may consist of continuum radiation and weak lines. The instrumental background is also present on those parts of the microchannel plate not illuminated by X-rays from the target source. We checked for any variation of the instrumental background perpendicular to the dispersion direction and found none. We then modeled this instrumental background bg along the dispersion direction by a low-order polynomial and found acceptable fits for almost the whole spectrum. A far more difficult task is the determination of a reliable source background sbg . The source background is by definition present only on the extracted spectral trace; it is formed by continuum radiation from the source, and possibly by weak, unrecognized spectral lines and/or higher order contamination.

For the determination of the fluxes of individual emission lines, the source background is required only in the vicinity of the line(s) under consideration and is

approximated by a single number. Our numerical procedures can, however, cope with arbitrary source background models. In order to estimate this source background, we adopted the following procedure. We first subtracted the instrumental background from the spectral trace on the source, and calculated the median of the thus obtained count values for all bins within the investigated (small) part of the spectrum. The median is a statistically robust estimate of the background (which we assume to be flat over the considered part of the spectrum) as long as more than 50% of all bins belong to the source background, i.e. the spectrum contains not too many lines. For each bin i we thus obtain a background value of $sbg + bg_i$ in the studied wavelength range.

4.4.2. Fit procedure

The emission line spectra are fitted with a maximum likelihood technique similar to that used by Schmitt et al. (1996a) for their EUVE spectra. The spectrum is assumed to consist of the background b and of M discrete emission lines. The treatment of the background b is described in Sect. 4.4.1. Each line j is assumed to be represented by a normalized profile $g_j(\lambda; \lambda_j, \sigma_j)$, e.g. a Gaussian profile

$$g_j(\lambda; \lambda_j, \sigma_j) = \frac{1}{\sqrt{2\pi}\sigma_j} e^{-\frac{(\lambda-\lambda_j)^2}{2\sigma_j^2}} \quad (6)$$

with the dispersion σ_j and the central wavelength λ_j . The assumption of a Gaussian line profile is of course arbitrary. Strong isolated emission lines (like O VIII Ly α) can be fitted quite well with such a model, and other analytical models can easily be incorporated into our scheme. Let the observed spectrum be given on a grid of N bins with wavelength values $\lambda_1 \dots \lambda_N$. The number of expected counts c_i in the i th bin can then be calculated as

$$c_i = sbg + bg_i + \sum_{j=1}^M a_j g_{i,j}, \quad (7)$$

where a_j is the total number of counts of line j and $g_{i,j}$ is the value of the profile function for line j in bin i . In order to compare the modeled spectrum c_i with a measured spectrum n_i , we assume n_i to be a Poisson realization of c_i . The total probability of the observations $n_1 \dots n_N$ is then given by

$$P(n_1 \dots n_N) = \prod_{i=1}^N e^{-c_i} \frac{c_i^{n_i}}{n_i!} \quad (8)$$

and the likelihood function $\mathcal{L}(a_j, \lambda_j, \sigma_j, j = 1 \dots N)$ is defined as

$$\mathcal{L} = -2 \ln P = -2 \sum_{i=1}^N (-c_i + n_i \ln c_i) + \text{const.} \quad (9)$$

The best-fit values of the parameters a_j , λ_j and σ_j ($j = 1 \dots N$) are determined by finding extremal values of \mathcal{L} through:

$$\frac{\partial \ln \mathcal{L}}{\partial a_j} = 0, \quad \frac{\partial \ln \mathcal{L}}{\partial \lambda_j} = 0, \quad \frac{\partial \ln \mathcal{L}}{\partial \sigma_j} = 0. \quad (10)$$

The physical meaning of the fit parameters a_j , λ_j and σ_j is quite different. λ_j and σ_j are in principle fixed by the wavelengths of the considered lines and the instrumental resolution, complications arise from possible wavelength calibration errors and line blends. On the other hand, the amplitudes a_j , proportional to the line flux, are the genuine interesting parameters. Analysis of the likelihood equations shows that for the amplitude a_j a fixed point equation can be derived for each line j with λ_j and σ_j assumed to be given:

$$a_{j,\text{new}} = \sum_{i=1}^N n_i \frac{a_{j,\text{old}} g_{i,j}}{c_{i,\text{old}}}. \quad (11)$$

Equation (11) can be efficiently solved by iteration. In order to find optimum values for the wavelengths λ_j and line-widths σ_j , we seek minimal values of \mathcal{L} by ordinary minimization procedures. In this process the wavelengths λ_j can vary either freely, or – if the wavelengths of the lines to be fitted are all known – the wavelength differences between the individual lines in a multiplet can be kept fixed in order to account for possible shifts of the overall wavelength scale. Similarly, the line widths σ_j can either vary freely or be fixed, and in such a way blended lines can be described. In this fashion an optimal value for \mathcal{L} is obtained, and the parameters a_j , λ_j (if fitted) and σ_j (if fitted) represent our best fit measurements of these values.

Measurement errors are determined by assuming the likelihood curve $\mathcal{L}(a_j)$ to be parabolic and finding the value of Δa_j where $\mathcal{L}(a_j \pm \Delta a_j) = \mathcal{L}(a_j) + d\mathcal{L}$ resulting in $\Delta a_j = \sqrt{2\Delta\mathcal{L}/\mathcal{L}''_j}$ with \mathcal{L}''_j being the second derivative of \mathcal{L} with respect to a_j known from Eqs. (9) and (7). We choose $\Delta\mathcal{L} = 1$ which yields formal 1σ errors.

Similarly the errors for λ_j and σ_j are calculated. We determine the errors in $d\lambda_j$ and $d\sigma_j$ numerically from $\mathcal{L}(\lambda_j)$ and $\mathcal{L}(\sigma_j)$, respectively with $\Delta\mathcal{L} = 1$, i.e. errors being given within 68.3%. Thus formally we treat all other parameters as “uninteresting”.

4.5. Extracted spectra and measured line ratios

With the procedure described in Sect. 4.4 we analyzed the spectra of the He-like triplets of O VII, N VI, and C V for the two stars Capella and Procyon. In Figs. 2 and 3 the measured spectra are plotted with bold line-dotted lines and the best-fit model curve is indicated by a thin solid line. The total background, i.e. the instrumental background and the assumed source continuum background, is shown with a dotted line. The derived best-fit parameters are given in Table 4, where we list, for both Capella and Procyon, the derived empirical wavelengths, the line widths and the line strengths (in counts). For reference purposes we also list the source background values used. Extrapolating the instrumental background onto the spectral trace shows that Procyon’s source background must be quite small as expected for a low coronal temperature X-ray source. It will therefore be neglected for the purpose of line flux modeling. In Table 4 we also list the

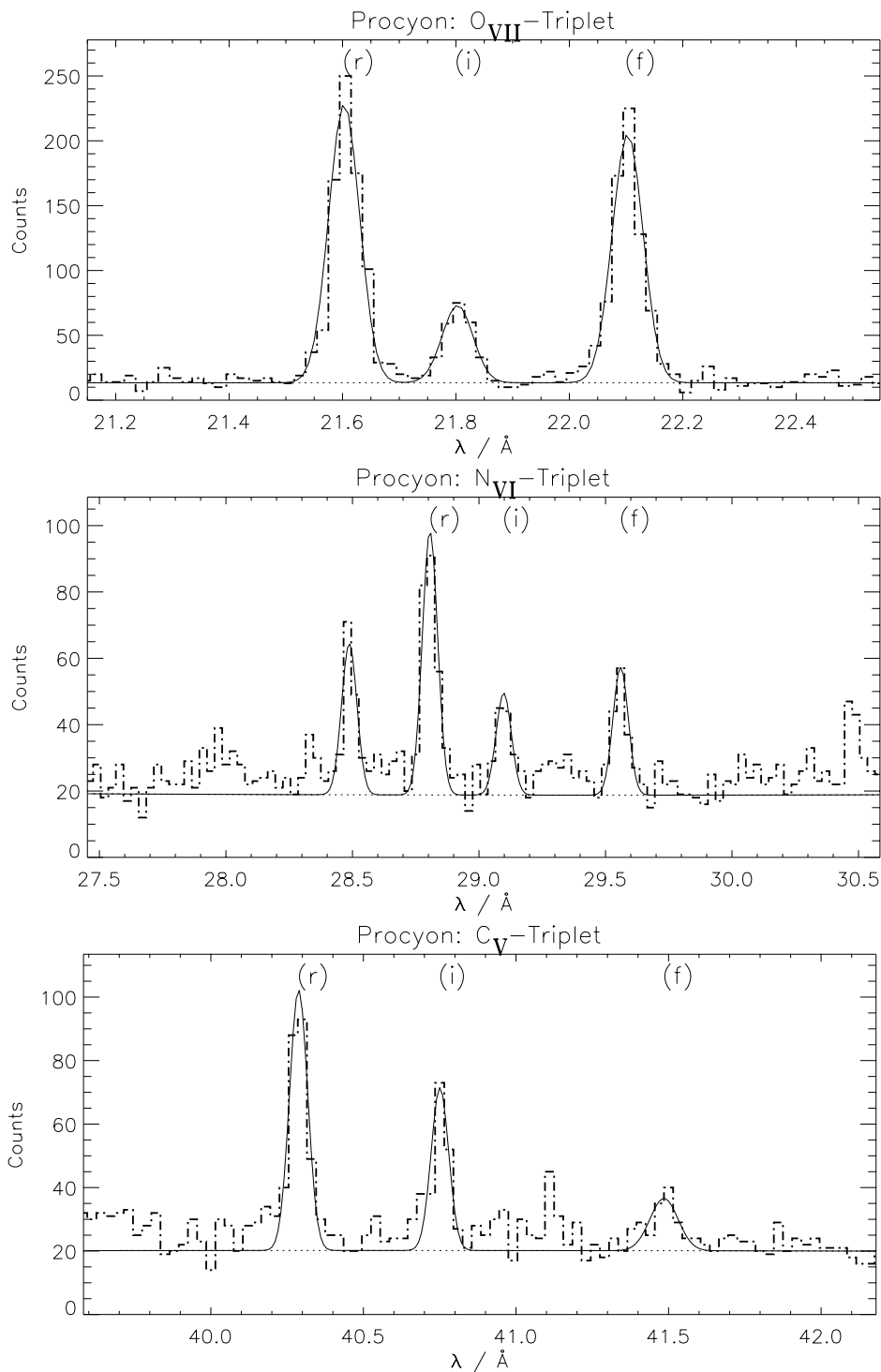


Fig. 2. Spectrum (line-dotted) and fitted (solid) curve for the O VII, N VI, and C V triplet for Procyon. The dotted line represents the total background. The binsize is 0.02 Å for O VII and 0.03 Å for C V and N VI

ratios between forbidden and intercombination line, and that of the sum of intercombination and forbidden line to the resonance line, which are needed for subsequent analysis. Since no significant rotational or orbital line broadening is expected given the even high spectral resolution of our *Chandra* data, the line-width σ was kept fixed for all models assuming that this value described the instrumental resolution. Starting values for the wavelengths were taken from Mewe et al. (1985).

The O VII triplet has the best signal to noise ratio in both stars and is unaffected by any significant contamination from higher orders as can be seen from Figs. 2 and 3 in the top panel. As far as the N VI triplet is concerned, it is not as isolated as the O VII triplet and requires further analysis. In both Procyon (Fig. 2) and Capella (Fig. 3) additional lines appear. At 28.44 Å a line attributed to C VI is evident for both Capella and Procyon. In order to minimize any possible cross talk, this line was

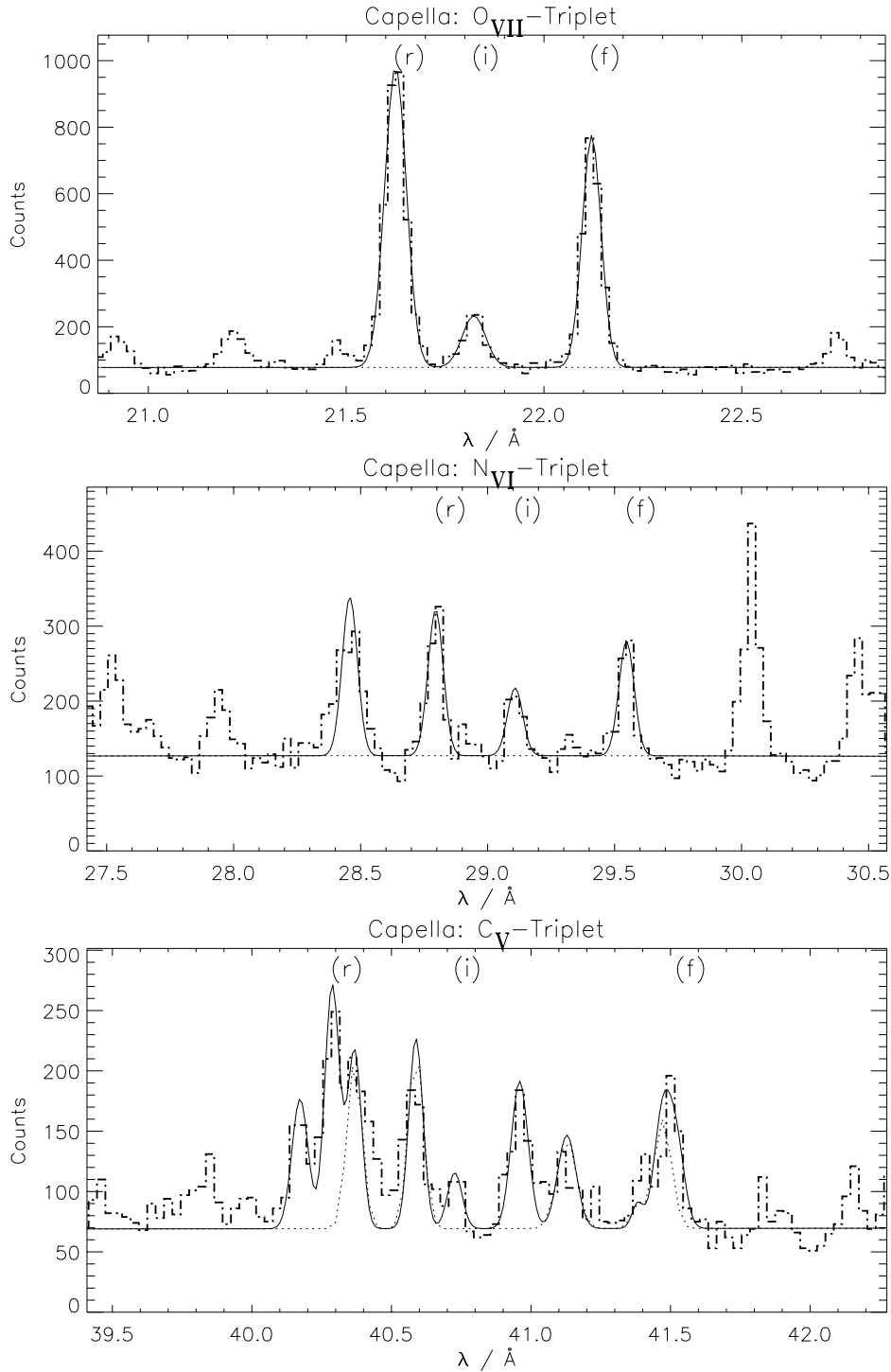


Fig. 3. Spectrum (line-dotted) and fitted (solid) curve for the O VII, N VI, and C V triplet for Capella. The dotted line represents the total background. The binsize is 0.02 Å for O VII and 0.03 Å for C V and N VI

included in the fit. The line at 30 Å seen in the Capella spectrum is interpreted as the second order of the strong Fe XVII line at 15.013 Å; Fe XVII is strong in Capella, but essentially absent in Procyon. A somewhat strange feature can be seen only in the N VI spectrum of Procyon at about 29.3 Å. This is not a line but an instrumental effect which is present only on the negative side of the spectrum.

4.5.1. Analysis of the C V triplet

Contamination with higher order lines makes the analysis of the C V triplet for Capella particularly difficult (cf., Fig. 3). This is clear since the Capella spectrum contains strong emission in the band between 13–14 Å, which appears in third order in the 39–42 Å band under consideration for the C V triplet. Specifically, the

Table 4. Measured line ratios for Capella and Procyon

Capella	λ [Å]	σ [Å]	A [cts]	sbg [cts/Å]	$R_{\text{obs}} = f/i$	$G_{\text{obs}} = \frac{i+f}{r}$
O VII						
<i>r</i>	21.62 ± 0.005		3071.2 ± 56.0			
<i>i</i>	21.82 ± 0.007	0.027	544.8 ± 31.4	2997	3.92 ± 0.24	0.87 ± 0.03
<i>f</i>	22.12 ± 0.001		2135.2 ± 51.1			
N VI						
<i>r</i>	28.79 ± 0.003		491.2 ± 31.49			
<i>i</i>	29.1 ± 0.004	0.03	228.2 ± 26.5	3265	1.68 ± 0.23	1.25 ± 0.14
<i>f</i>	29.54 ± 0.003		384.5 ± 29.4			
C V						
<i>r</i>	40.28 ± 0.002	0.026	440.7 ± 26.9			
<i>i</i>	40.72 ± 0.008	0.026	101.3 ± 18.24	1200	1.58 ± 0.36	0.59 ± 0.1
<i>f</i>	41.5 ± 0.005	0.029	160.2 ± 22.37			
Procyon						
O VII						
<i>r</i>	21.6 ± 0.006		731.6 ± 28.7			
<i>i</i>	21.8 ± 0.004	0.027	203 ± 16.8	0	3.21 ± 0.3	1.17 ± 0.08
<i>f</i>	22.1 ± 0.003		652.4 ± 27.3			
N VI						
<i>r</i>	28.8 ± 0.003		200.2 ± 16.8			
<i>i</i>	29.1 ± 0.006	0.03	77.4 ± 12.3	0	1.26 ± 0.26	0.87 ± 0.14
<i>f</i>	29.55 ± 0.005		97.1 ± 13.2			
C V						
<i>r</i>	40.28 ± 0.003	0.03	203.8 ± 17.0			
<i>i</i>	40.75 ± 0.004	0.028	123.1 ± 14.2	0	0.51 ± 0.12	0.92 ± 0.16
<i>f</i>	41.48 ± 0.01	0.046	63.4 ± 13.5			

interfering lines are Ne IX ($13.44 \text{ \AA} \times 3 = 40.32 \text{ \AA}$), Fe XIX ($13.52 \text{ \AA} \times 3 = 40.56 \text{ \AA}$), Ne IX ($13.7 \text{ \AA} \times 3 = 41.1 \text{ \AA}$), Fe XIX ($13.795 \text{ \AA} \times 3 = 41.385 \text{ \AA}$) and Fe XVII ($13.824 \text{ \AA} \times 3 = 41.472 \text{ \AA}$). We modeled the contamination from these five lines by first determining their first order contributions, transforming the fit results to third order. In the transformation the first order intensities are reduced by a factor of 14.1. This reduction factor is obtained by comparison of first and third order of the isolated 15.013 \AA line (Fe XVII). Since the contaminating photons are rather energetic, we expect essentially the same reduction factor in the range $13\text{--}14 \text{ \AA}$. The first order fit result is plotted in Fig. 4 and the resulting fit values are listed in Table 5. Technically the higher order contamination was treated as an additional non-constant contribution to the instrumental background. In addition to the C V triplet, another line, Si XII at 40.91 \AA , appearing strong in Capella but weaker in Procyon, had to be modeled. The source background was estimated by requiring the lowest count bins to be adequately modeled. The median function could not be applied since there are too many lines in the considered wavelength range. The result of this modeling exercise is shown in Fig. 3 in the bottom panel, where the dotted line, representing

the background, is not constant, but heavily influenced by higher order lines. We emphasise that the errors listed in Table 4 do not include errors from the fits in the 13 \AA band. We point out in particular that the forbidden C V line lies on top of the third order Fe XVII 13.824 \AA line, so that any derivation of the forbidden line flux does require an appropriate modeling of the third order contamination. This is especially difficult because the Fe XVII 13.824 \AA line is blended with the Fe XIX 13.795 \AA line in first order, while in third order this blend is resolved.

The strong emission in the 13 \AA regime is mostly due to iron in excitation stages Fe XVII and Fe XIX. Since there is no significant emission from iron in these high excitation stages in the spectrum of Procyon, there is no blending with third order lines in this case. From Fig. 2 it can be seen that the modeling is straightforward for Procyon.

5. Results and interpretation

Inspection of our Chandra spectra of Capella and Procyon shows the O VII and N VI forbidden lines to be present in both cases. The C V forbidden line is very weak but present

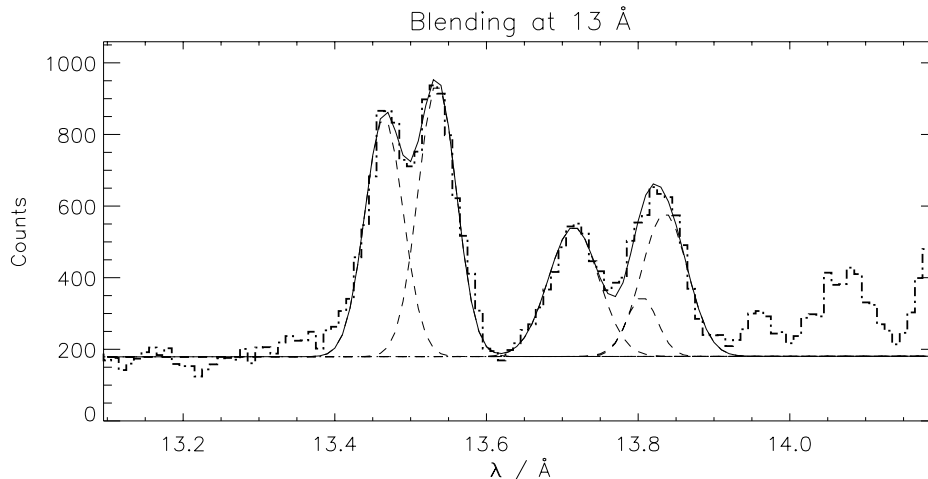


Fig. 4. First order spectrum responsible for third order contamination of the C v triplet of Capella; shown are the data (dash-dotted histogram) as well as the best fit (solid line). Note that the feature near 13.8 Å is actually a line blend (consisting of Fe XIX and Fe XVII contributions) resolved in third order

Table 5. Fit result in the 13–14 Å range for Capella. The assumed source background is 5792 cts/Å

Line	λ [Å]	σ [Å]	A [cts]
Ne IX	13.46 ± 0.003	0.025	4373.9 ± 82.92
Fe XIX	13.53 ± 0.001	0.025	4683.4 ± 84.52
Ne IX	13.71 ± 0.004	0.033	3019.9 ± 74.50
Fe XIX	13.8 ± 0.02	0.02	496.6 ± 62.06
Fe XVII	13.83 ± 0.008	0.03	3337.6 ± 77.94

for Procyon, it is also present in Capella despite being significantly contaminated by third order radiation. The observed f/i -ratios for O VII are very close to the expected low-density limit R_0 for both Procyon and Capella, while the measured f/i -ratios for N VI and C V are definitely below the respective values of R_0 in both cases. Before giving a quantitative interpretation of the observed line ratios we must first consider the formation temperature of the studied He-like lines. Especially for the C V triplet the stellar radiation field can contribute significantly to the depopulation of the atomic level from which the forbidden line originates. Low forbidden line intensities can thus also indicate large radiation fields and not necessarily high densities.

5.1. Formation temperature of lines

For the purpose of density diagnostics it is customary to assume that all of the emission is produced at a single temperature T_m (cf., Table 2), which corresponds to the peak of the contribution function of the considered line, the so-called formation temperature. It should be kept in mind, however, that He-like ions are present over a relatively broad temperature range, and therefore this

assumption might be poor if steep emission measure gradients are present. The measured value of G is also a temperature diagnostics, although optical depth effects in the resonance line may contribute (cf., Acton 1978); the relevance of optical depth effects to our results is analyzed in Sect. 5.4. In Table 6 we show the temperatures $T(G)$ determined from converting the observed G_{obs} values into temperatures according to Mewe et al. (2000a) using an electron density of $n_e = 5 \cdot 10^9 \text{ cm}^{-3}$. We also determined temperatures by studying the line ratio between the observed Ly α lines of O VIII, N VII, and C VI and the r-lines of O VII, N VI, and C V respectively by assuming isothermal plasma emission. We assume plasma emissivities as calculated in the codes MEKAL (Mewe et al. 1985; Mewe et al. 1995) and SPEX (Kaastra et al. 1996). The thus obtained fluxes are multiplied with effective areas (cf., Table 7) before comparison with the measured ratios. The results are listed in Table 6 as $T(\text{H-He})$.

As can be seen from Table 6, the temperatures $T(G)$ and $T(\text{H-He})$ do not agree. This is not surprising given the fact that we are likely dealing with a temperature distribution. For Procyon the temperatures $T(\text{H-He})$ agree quite well with T_m , while $T(G)$ agrees with T_m only for N VI. For Capella the respective temperatures $T(\text{H-He})$ always exceed those found for Procyon, while the $T(G)$ temperature derived from N VI is below that found for Procyon. We tentatively conclude that the observed N VI and O VII emission in Capella has significant contributions from plasma at temperatures away from the peak in the line emissivity curve, while for Procyon the emission appears to come from rather close to the line emissivity peak.

5.2. Influence of the stellar radiation field

The observed C V line ratios are particularly interesting. While the observed value for Capella agrees well with

Table 6. Temperature diagnostics from ratio of Ly_{α}/r and from the ratio $G = (i + f)/r$. Values for r and G are taken from Table 4 (the G values listed are corrected for effective areas; cf., Table 7). For comparison the peak line formation temperature T_m is also given. $T(G)$ is calculated according to Mewe et al. (2000a)

Ion	λ [Å]	Procyon [cts]	Capella [cts]
C VI (cts)	33.75	697.5 ± 28.1	2151.1 ± 51.3
C V (cts)	40.27	203.8 ± 17.0	440.7 ± 26.9
C VI/C V		3.42 ± 0.32	4.88 ± 0.41
$T(\text{H-He})/\text{MK}$		1.14 ± 0.03	1.27 ± 0.03
G_{obs}		1.27 ± 0.21	0.81 ± 0.14
$T(G)/\text{MK}$		0.32 ± 0.15	0.98 ± 0.43
T_m/MK		1.0	1.0
N VII (cts)	24.8	206.9 ± 16.95	2280.3 ± 53.6
N VI (cts)	28.79	200.2 ± 16.8	491.2 ± 31.49
N VII/N VI		1.03 ± 0.12	4.64 ± 0.41
$T(\text{H-He})/\text{MK}$		1.5 ± 0.05	2.5 ± 0.08
G_{obs}		0.93 ± 0.16	1.33 ± 0.15
$T(G)/\text{MK}$		1.25 ± 0.60	0.47 ± 0.17
T_m/MK		1.4	1.4
O VIII (cts)	18.97	673.2 ± 27.6	14676.8 ± 124.3
O VII (cts)	21.6	731.6 ± 28.7	3071.2 ± 56
O VIII/O VII		0.92 ± 0.05	4.78 ± 0.13
$T(\text{H-He})/\text{MK}$		2.13 ± 0.03	3.4 ± 0.03
G_{obs}		1.21 ± 0.08	0.90 ± 0.03
$T(G)/\text{MK}$		1.0 ± 0.16	2.01 ± 0.16
T_m/MK		2.0	2.0

the solar observations (cf., Austin et al. 1966; Freeman & Jones 1970), the observed value for Procyon is rather small. The important point to keep in mind in this context is that Procyon and Capella are stars with different properties compared to the Sun. Procyon is of spectral type F5V-IV (cf., Table 1) with an effective temperature of 6500 K, Capella is a spectroscopic binary, the components of which are of spectral type G1 and G8; occasionally the brighter component is also classified as F9. Strictly speaking, what really matters is the effective temperature of the radiation field at the wavelength corresponding to the energy difference between forbidden and intercombination line levels, i.e., 2272 Å for C V (cf., Table 8) for the transition $2^3\text{P} \rightarrow 2^3\text{S}$. We investigated the stellar surface radiation fluxes from measurements obtained with the International Ultraviolet Explorer satellite (IUE). We first determined continuum fluxes from archival IUE data, and converted these fluxes into intensities using the expression

$$I_{\lambda} = F_{\lambda} \frac{d^2}{R^2} \frac{1}{2\pi(1 - \epsilon)}, \quad (12)$$

where ϵ is the (linear) limb darkening coefficient. It is determined from (1995) using $\log g$ and T_{eff} listed in Table 1;

Table 7. Effective areas of the detector at the designated wavelengths. The values are taken from In-Flight Calibration by Deron Pease (9 March 2000)

element	$\lambda / \text{Å}$	$A_{\text{eff}} / \text{cm}^2$		
		λ_+	λ_-	total
C VI	33.76	5.09	5.09	10.18
C V (r)	40.28	2.34	2.34	4.68
C V (i)	40.74	1.65	1.65	3.30
C V (f)	41.5	1.76	1.76	3.52
N VII	24.8	7.76	7.75	15.51
N VI (r)	28.8	6.34	6.33	12.67
N VI (i)	29.1	6.16	6.15	12.31
N VI (f)	29.54	5.80	5.79	11.59
O VIII	18.98	10.08	10.70	20.78
O VII (r)	21.62	6.47	7.05	13.52
O VII (i)	21.82	6.36	6.94	13.30
O VII (f)	22.12	6.22	6.81	13.03

d and R are distance and radius of the sample stars as listed in Table 1. For the case of the binary system Capella we assumed the worst case and attributed all emission to the Ab component, i.e., the star with the higher radiation temperature. The other component Aa (G8/K0 III) is about equally bright in the corona as G1 III (cf., Linsky et al. 1998), but much weaker in the chromosphere and transition region. From the thus obtained value for the intensity a radiation temperature T_{rad} can be inferred from the appropriate Planck curve, expressed as

$$u_{\nu} = W \frac{8\pi h\nu^3}{c^3} \frac{1}{\exp\left(\frac{h\nu}{kT_{\text{rad}}}\right) - 1}, \quad (13)$$

where W is the dilution factor of the radiation field (we take $W = \frac{1}{2}$ close to the stellar surface). The results derived from these data are listed in Table 8.

In order to compute the dependence of ϕ/ϕ_c , required in Eq. (2), on T_{rad} we use the calculations by Blumenthal et al. (1972), who derive the expression

$$\frac{\phi}{\phi_c} = \frac{3(1+F)c^3}{8\pi h\nu^3} \frac{A(2^3\text{P} \rightarrow 2^3\text{S})}{A(2^3\text{S}_1 \rightarrow 1^1\text{S}_0)} u_{\nu} \quad (14)$$

with $\phi_c = A(2^3\text{S}_1 \rightarrow 1^1\text{S}_0)/(1+F)$, transition probabilities $A(i \rightarrow j)$, and u_{ν} the spectral energy density at the appropriate $2^3\text{P}_1 \rightarrow 2^3\text{S}_1$ frequency ν . The factor 3 is the ratio of the statistical weights of the levels 2^3P and 2^3S . F is approximated by Blumenthal et al. (1972) through

$$F(\xi) = \frac{3\xi H(\xi) \exp(\xi/4) + 1.2\xi + 2H(\xi) + 2}{3\xi \exp(\xi/4) + 0.6\xi H(\xi) + H(\xi) + 1}, \quad (15)$$

where

$$H(\xi) = \frac{C(1^1\text{S} \rightarrow 2^3\text{S})}{C(1^1\text{S} \rightarrow 2^3\text{P})}, \quad (16)$$

with $\xi = I/kT_{\text{rad}}$ and the collisional excitation rate coefficients $C(i \rightarrow j)$. The ionization potentials I_{pot} for

Table 8. Investigation of the influence of the stellar radiation field. Measured fluxes from the IUE satellite F_λ are converted to intensity I_λ taking into account limb darkening effects using ϵ from Table 1

	C V	N VI	O VII
$\lambda_{f \rightarrow i}/\text{\AA}$	2272	1900	1630
I_{pot}/eV	392.1	552.1	739.3
Capella			
$F_\lambda/(10^{-11} \frac{\text{ergs}}{\text{cm}^2 \text{s \AA}})$	2 ± 0.5	1.2 ± 0.5	0.25 ± 0.05
$I_\lambda/(10^4 \frac{\text{ergs}}{\text{cm}^2 \text{s \AA strd}})$	1.98 ± 0.5	1.19 ± 0.3	0.25 ± 0.5
T_{rad}/K	4585 ± 100	4976 ± 150	5029 ± 50
ϕ/ϕ_c	2.54 ± 0.86	0.2 ± 0.1	0.003 ± 0.0005
Procyon			
$F_\lambda/(10^{-11} \frac{\text{ergs}}{\text{cm}^2 \text{s \AA}})$	15 ± 4	7 ± 3	0.6 ± 0.3
$I_\lambda/(10^4 \frac{\text{ergs}}{\text{cm}^2 \text{s \AA strd}})$	21 ± 5	9.8 ± 4	0.84 ± 0.4
T_{rad}/K	5532 ± 150	5778 ± 200	5406 ± 300
ϕ/ϕ_c	26.67 ± 9.3	1.58 ± 0.84	0.01 ± 0.015
$\phi_c/(\text{s}^{-1})$	34.6	148	717

the ions C V, N VI, and O VII are taken from Pradhan & Shull (1981). The collisional excitation rate coefficients $C(i \rightarrow j)$ were taken from Pradhan et al. (1981) for C V and O VII while the rate coefficients for N VI were obtained by interpolation from these values.

From Eq. (14) we determine the values used in Eq. (2) for the calculation of the theoretical curves in Fig. 5. They are also listed in Table 8. For comparison, we also give in Table 8 the values derived from recent calculations by Mewe et al. (2000a) considering a multi-level model previously used by Porquet & Dubau (2000), and taking into account the effect of temperature on G and $R(n_e)$ (Mewe et al. 2000a, see also Porquet & Dubau 2000).

5.3. Analysis and interpretation

In Fig. 5 we show for Procyon and Capella the expected line ratio f/i as a function of the electron density n_e in comparison with the observed line ratio R_{obs} (corrected for detector efficiencies) and its 1σ error. The expected curves are plotted for the radiation temperature range estimated for the two stars as listed in Table 8; for O VII the stellar radiation field does not significantly influence the f/i ratio as expected. We used the formation temperatures $T(G)$ calculated from the G ratios as listed in Table 6, thus assuming all the emission being produced at a single temperature. In Table 9 we summarize the derived densities and their 1σ errors for Procyon and Capella not accounting for errors in $T(G)$. No density values could be determined for the C V triplet in Procyon and for the O VII triplet in Capella. Instead we give upper limits for the two cases (Table 9); for Capella only a 2σ upper limit could be determined.

Table 9. Results of density diagnostics

$\log n_e/\text{cm}^{-3}$	Capella	Procyon
C V	9.42 ± 0.21	< 8.92
N VI	9.86 ± 0.12	9.96 ± 0.23
O VII	< 9.38 (2σ upper limit)	$9.28^{+0.4}_{-9.28}$

Obviously, for both stars the measured line ratios are within (Capella) and very close to (Procyon) the low-density limit R_0 . At any rate, the measured f/i ratio is larger for Capella than for Procyon, so one arrives at the somewhat unexpected conclusion that the coronal density in the active star Capella should be smaller than in the inactive star Procyon.

5.4. Optical depth effects

In all of the above analysis we assumed all triplet lines to be optically thin. In the following section we show this assumption to be consistent with our results. Let us therefore assume that the optical depth in the resonance lines is not small. This leads to a reduction of the measured resonance line flux due to radiative scattering. At line center the optical depth is given by the equation

$$\tau = 1.2 \cdot 10^{-17} \left(\frac{n_i}{n_{\text{el}}} \right) A_z \left(\frac{n_{\text{H}}}{n_e} \right) \lambda f \sqrt{\frac{M}{T}} n_e \ell \quad (17)$$

(Schrijver et al. 1994) with the fractional ionization is denoted by n_i/n_{el} , the elemental abundances by A_z , the ratio of hydrogen to electron density is $n_{\text{H}}/n_e = 0.85$, the oscillator strength $f = 0.7$ for all ions, the atomic number is M , the wavelength is measured in \AA , the temperature in K, the electron density n_e in cm^{-3} and the mean free path is denoted by ℓ . In Eq. (17) we adopt a value of unity for the fractional ionization and use the solar abundances. We further assume T at the peak line formation and note, that τ is rather insensitive to the precise value of T . We can determine – for each resonance line – that value of $n_e \ell$ which yields an optical depth of unity. Adopting a maximum value of n_e of 10^{10} cm^{-3} (cf. Table 9), we determine lower values of ℓ of $1.3 \cdot 10^{12} \text{ cm}$, $5.6 \cdot 10^{12} \text{ cm}$ and $6.0 \cdot 10^{11} \text{ cm}$, for O VII, N VI and C V, respectively. Assuming a geometry most suitable for resonance scattering, we can compute the respective emission measures of $n_e^2 \ell^3$ respectively. Comparing these emission measures with those derived from the measured line fluxes f_λ

$$EM = \frac{4\pi d^2 f_\lambda}{p_\lambda(T)} \quad (18)$$

with the line cooling function $p_\lambda(T)$ and the distance d (cf. Table 1), shows the former to be larger by a few orders of magnitude for both stars. This inconsistency shows that the assumption of a non-negligible optical depth is invalid and we conclude that optical depth effects are irrelevant for the analysis of He-like triplets in Procyon and Capella.

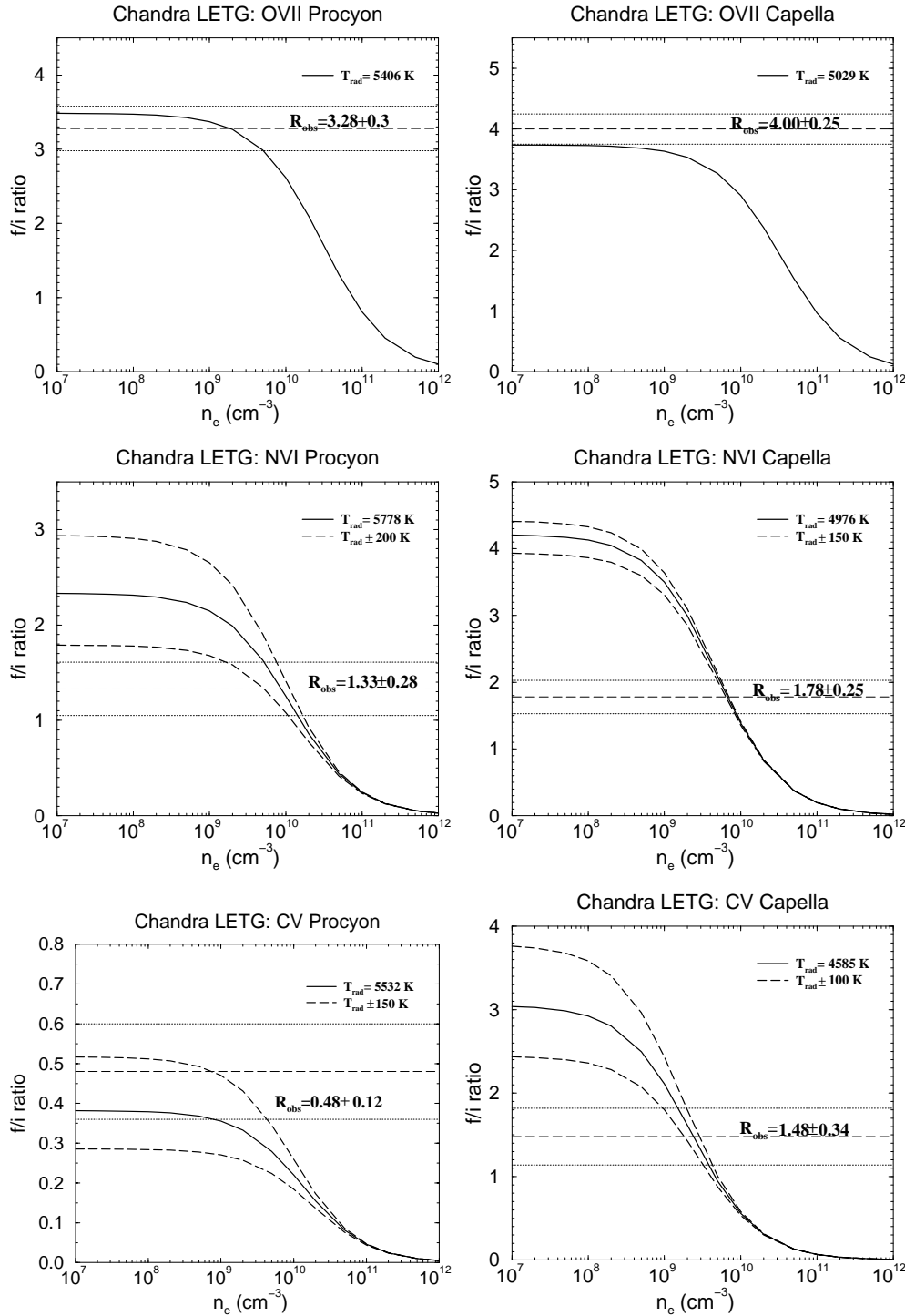


Fig. 5. Theoretical curves in the radiation temperature range given in Table 8 in comparison with the measured value of R_{Obs} for the O VII, N VI and the C V triplet for Capella and Procyon. The measured R values from Table 4 are corrected for detector efficiencies

6. Conclusions

6.1. Comparison with the Sun

Both Capella and Procyon are considered to be solar-like stars. In the solar context the He-like triplets of oxygen, nitrogen and carbon have been known for a long time and

in fact the He-like ion density diagnostics have been first developed to interpret these solar data. Many solar observations are available for the O VII triplet, while only very few observations have been made for the N VI and C V triplets. The first observations of the C V triplet are reported by Austin et al. (1966), who obtained an f/i -ratio

(at most a factor of 2) in Capella as compared to Procyon. As a consequence we must have $p_{\text{Procyon}} \approx p_{\text{Capella}}$ for the gas pressures in the respective line forming regions. Capella's peak coronal temperature is clearly much higher than Procyon's. If we again assume – going along with the solar analogy – that for both Procyon and Capella (all of) the X-ray emission originates from magnetically confined plasma loops, the loop top temperatures in Capella must be higher than in Procyon. The loop scaling laws then imply for the typical loop length scales L for Procyon and Capella $\frac{L_{\text{Capella}}}{L_{\text{Procyon}}} = \left(\frac{T_{\text{max, Capella}}}{T_{\text{max, Procyon}}}\right)^3$. A conservative estimate yields $\frac{T_{\text{max, Capella}}}{T_{\text{max, Procyon}}} > 2$, thus $L_{\text{Capella}} \geq 8 L_{\text{Procyon}}$. The conclusion then appears inescapable that the typical sizes of the magnetic structures in Procyon and Capella are quite different by probably at least one order of magnitude.

Next, it is instructive to compare the total mean surface fluxes emitted in the helium- and hydrogen-like ions of carbon, nitrogen and oxygen for Procyon and Capella. Using the measured count ratios and correcting for the effects of distance, exposure times and the surface areas of the stars we find for the C V, C VI, N VI, N VII, O VII, and O VIII lines values of (Capella)/(Procyon) of 0.96, 1.37, 1.09, 4.9, 1.87, and 9.71 respectively. Therefore up to those temperatures where the C V, C VI, and N VI lines are formed, the mean surface fluxes in the two stars hardly differ at all; pressures and temperatures are also quite similar. We therefore conclude that the physical characteristics and global properties (such as filling factor) of Procyon's and Capella's corona at a level of $T \sim 10^6$ K are very similar.

It is interesting to again perform a comparison to the Sun. Freeman & Jones (1970) quote – for their SL801 rocket flight on Nov. 20 1969 – resonance line fluxes of $4.2 \cdot 10^{-3}$, $2.1 \cdot 10^{-3}$, and $3.1 \cdot 10^{-3}$ erg/(cm²s) for O VII, N VI, and C V respectively. Correcting for the distance between Earth and Sun we find average surface fluxes of 200, 100, and 150 erg/cm²/s for O VII, N VI, and C V respectively on the solar surface. Carrying out the same calculation for our *Chandra* data, we find – using the effective areas given in Table 7 – mean surface fluxes in O VII of 3700 and 1980 erg/(cm²s), in N VI of 480 and 430 erg/(cm²s), and in C V of 830 and 860 erg/(cm²s) for Capella and Procyon respectively. We therefore recover our previous finding that Capella's and Procyon's surface fluxes are quite similar, and determine in addition that both stars exceed typical (?) solar values by one order of magnitude. Since the physical conditions of the line emitting regions are quite similar, we conclude that the coronal filling factors are larger.

Evaluating now the coronal pressure for Procyon we find – using the densities and temperatures derived from N VI – $p(\text{N VI}) = 4.4$ dyn/cm², a value also very typical for solar active regions. From the loop scaling law (Rosner et al. (1978)) $T_{\text{max}} = 1.4 \cdot 10^3 (pL)^{(1/3)}$ we deduce a typical length of $2.7 \cdot 10^8$ cm using $T_{\text{max}} = 1.5 \cdot 10^6$ K. This value must be considered as a lower limit to the probable

length scale because of the unfortunate sensitive dependence of L on T_{max} through $L \sim T_{\text{max}}^3$; T_{max} is likely somewhat higher than $T_{\text{max}} = 1.5 \cdot 10^6$ K as suggested by the temperatures derived from the O VIII data. At any rate, however, the conclusion is, that the X-ray emission originates from low-lying loops and hence also our *Chandra* data support the view that Procyon's corona has an appearance very similar to the Sun's, just like the conclusion drawn by Schmitt et al. (1996b) from their EUVE spectra. It then follows that the sizes of the magnetic loops in Procyon's corona are similar to the loops found in the solar corona. Adopting – for argument's sake – a characteristic length of $L_{\text{Proc}} = 1 \cdot 10^9$ cm, we then find for Capella $L_{\text{Capella}} > 8 \cdot 10^9$ cm, and possibly even a significant fraction of Capella's radius. This result is somewhat puzzling. On the Sun, loop structures, i.e., magnetically closed topologies, are occasionally found at larger heights, but they are always of low density and they never contribute significantly to the overall X-ray emission. It will be interesting to see whether this behavior is typical for active stars in general, or whether it applies only to Capella. After all, Capella may not be the prototypical active star. Its corona is not as hot as that of other stars, it does not produce flares and its radio emission is very weak.

Acknowledgements. J.-U. N. acknowledges financial support from Deutsches Zentrum für Luft- und Raumfahrt E. V. (DLR) under 50OR98010. The Space Research Organization Netherlands (SRON) is supported financially by NWO. We thank Tom Ayres, U/COLORADO (CASA), for very useful discussion.

References

- Acton, L. W. 1978, ApJ, 255, 1069
- Austin, W. E., Purcell, J. D., Tousey, R., & Widing, K. G., ApJ, 145, 373
- Blumenthal, G. R., Drake, G. W., & Tucker, W. H. 1972 ApJ, 172, 205
- Brinkman, A. C., Gunsing, C. J. T., Kaastra, J. S., et al. 2000, ApJ, 530, L111
- Brown, W. A., Bruner, M. E., Acton, L. W., et al. 1986 ApJ, 301, 981
- Catura, R. C., Acton, L. W., & Johnson, H. M. 1975, ApJL, 196, L47
- Díaz-Cordovés, J., Claret, A., & Giménez, A. 1995, A&AS, 110, 329
- Doyle, J. G. 1980, A&A, 87, 183
- Drake, J. J., Laming, J. M., & Widing, K. G. 1995, ApJ, 443, 393
- Dupree, A. K., Brickhouse, N. S., Doschek, G. A., et al. 1993, ApJL, 418, L41
- Freeman, F. F., & Jones, B. B. 1970, Sol. Phys., 15, 288
- Fuhrman, K., Pfeiffer, M., Frank, C., et al. 1997, A&A, 323, 909
- Gabriel, A. H., & Jordan, C. 1969, MNRAS, 145, 241
- Hummel, C. A., Armstrong, J. T., Quirrenbach, A., et al. 1994, ApJ, 107(5), 1859
- Hünsch, M., Schmitt, J. H. M. M., & Voges, W. 1998a, A&A, 127, 251

- Hünsch, M., Schmitt, J. H. M. M., & Voges, W. 1998b, *A&A*, 132, 155
- Irwin, A. W., Fletcher, J. M., Yang, S. L. S., et al. 1992, *PASP*, 104, 489
- Kaastra, J. S., Mewe, R., & Nieuwenhijzen, H. 1996, in *UV and X-ray Spectroscopy of Astrophysical and Laboratory Plasmas*, ed. K. Yamashita, & T. Watanabe (Tokyo, Universal Academy Press, Inc.), 411 (SPEX)
- Kelch, W. L., Linsky, J. L., Basri, G. S., et al. 1978, *ApJ*, 220, 962
- Lemen, J. R., Mewe, R., Schrijver, C. J., et al. 1989, *ApJ*, 341, 474
- Linsky, L. L., Wood, B. E., Brown, A., et al. 1998, *ApJ*, 492, 767
- McKenzie, D. L., Ruge, H. R., Underwood, J. H., et al. 1978, *ApJ*, 221, 342
- McKenzie, D. L., & Landecker, P. B. 1982, *ApJ*, 259, 372
- Mewe, R., & Schrijver, J. 1978, *A&A* 65, 114
- Mewe, R., Heise, J., Gronenschild, E. H. B. M., et al. 1975, *ApJL*, 202, L67
- Mewe, R., Gronenschild, E. H. B. M., Westergaard, N. J., et al. 1982, *ApJ*, 260, 233
- Mewe, R., Gronenschild, E. H. B. M., & van den Oord, G. H. J. 1985, *A&AS*, 62, 197
- Mewe, R., Schrijver, C. J., Lemen, J. R., et al. 1986, *Adv. Space Res.*, 6, 133
- Mewe, R., Kaastra, J. S., & Liedahl, D. A. 1995, *Legacy*, 6, 16 (MEKAL)
- Mewe, R., Porquet, D., Raassen, A. J. J., & Kaastra, J. S. 2000a, in preparation
- Mewe, R., Raassen, A. J. J., Brickhouse, N. S., et al. 2000b, *A&A*, submitted
- Parkinson, J. H. 1975, *Sol. Phys.*, 42, 183
- Porquet, & Dubau 2000, *A&AS*, 143, 495
- Pradhan, A. K. 1982, *ApJ*, 263, 477
- Pradhan, A. K. 1985, *ApJ*, 288, 824
- Pradhan, A. K., Norcross, D. W., & Hummer, D. G. 1981, *ApJ*, 246, 1031
- Pradhan, A. K., & Shull, J. M. 1981, *ApJ*, 249, 821
- Predehl, P., Braeuninger, H., Brinkman, A., et al. 1997, *Proc. SPIE*, 3113, 172
- Rosner, R., Tucker, W. H., & Vaiana, G. S. 1978, *ApJ*, 220, 643
- Schmitt, J. H. M. M., Harnden, F. R., Jr., Rosner, R., et al. 1985, *ApJ*, 288, 751
- Schmitt, J. H. M. M., Haisch, B. M., & Drake, J. J. 1994, *Science*, 265, 1420
- Schmitt, J. H. M. M., Drake, J. J., Stern, R. A., et al. 1996a, *ApJ*, 457, 882
- Schmitt, J. H. M. M., Drake, J. J., Haisch, B. M., et al. 1996b, *ApJ*, 467, 841
- Schmitt, J. H. M. M. 1997, *A&A*, 318, 215
- Schrijver, C. J., van den Oord, G. H. J., & Mewe, R. 1994, *A&A*, 289, L23
- Schrijver, C. J., van den Oord, G. H. J., Mewe, R., et al. 1995, *A&A*, 302, 438
- Vaiana, G. S., Cassinelli, J. P., & Giacconi, R. 1981, *ApJ*, 244, 163
- Vedder, P. W., & Canizares, C. R. 1983, *ApJ*, 270, 666